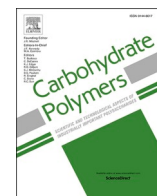| Title	Chitosan/acetoacetylated poly(vinyl alcohol) nanofibers incorporating starch-derived carbon quantum dots with pH-responsive color change for wound dressings
Author(s)	Yao, Ying; Hsu, Yu I.; Sonntag, Selina et al.
Citation	Carbohydrate Polymers. 2025, 371, p. 124477
Version Type	VoR
URL	https://hdl.handle.net/11094/103290
rights	This article is licensed under a Creative Commons Attribution-NonCommercial-NoDerivatives 4.0 International License.
Note	

Chitosan/acetoacetylated poly(vinyl alcohol) nanofibers incorporating starch-derived carbon quantum dots with pH-responsive color change for wound dressings

Ying Yao [a], Yu-I Hsu [a,*], Selina Sonntag [b], Alicia Fernández-Colino [b], Stefan Jockenhövel [b], Hiroshi Uyama [a,*]

[a] *Department of Applied Chemistry, Graduate School of Engineering, The University of Osaka, 2-1 Yamadaoka, Suita, Osaka 565-0871, Japan*
[b] *Department of Biohybrid & Medical Textile (BioTex), Center for Biohybrid Medical Systems (CBMS), Institute for Applied Medical Engineering, RWTH Aachen University, Forckenbeckstr. 55, 52074, Aachen, Germany*

ABSTRACT

Monitoring wound healing status through pH-responsive visual cues is essential for the effective management of chronic wounds. In this study, we developed biomass-derived carbon quantum dots (CQDs) using hydroxypropyl starch as the carbon source via a simple, eco-friendly synthesis strategy. Composite nanofibrous dressings were subsequently fabricated by incorporating CQDs with acetoacetylated polyvinyl alcohol (AAPVA) and chitosan (CS) through electrospinning. The resulting CQDs/CS/AAPVA nanofibers exhibited pronounced optical responsiveness within the pH range of 5–8, displaying visible color and fluorescence changes under visible and ultraviolet light. Furthermore, quantitative pH detection was achieved through RGB image analysis, demonstrating strong practical potential for wound monitoring. Owing to the synergistic effects between CQDs and CS, the composite nanofibers also exhibited excellent mechanical strength (Tensile stress $= 10.0 \pm 1.2$ MPa), high swelling capacity ($\sim 619.4 \pm 26.8$ %), structural stability, and biocompatibility, underscoring their significant promise for intelligent chronic wound management and remote monitoring.

1. Introduction

With the growing challenges posed by population aging, diabetes, and infection-related complications, skin injuries resulting from diabetic foot ulcers, burns, and other conditions frequently progress into chronic wounds (Uberoi et al., 2024; Versey et al., 2021). These wounds are characterized by slow healing and high susceptibility to infection, significantly compromising patients' quality of life and imposing a substantial socioeconomic and healthcare burden (Chen et al., 2024; Xiong et al., 2024). Although frequent debridement and dressing changes are clinically beneficial for infection control, they may also disrupt newly formed tissue, delay healing, and increase the risk of secondary infections (Long et al., 2022; Shi et al., 2024). Therefore, the development of smart wound dressings capable of non-invasively indicating wound status has become a key research focus, as such dressings could enable real-time monitoring and reduce unnecessary interventions, ultimately improving patient comfort and care efficiency (Li et al., 2025; Percival et al., 2014).

Different stages of wound healing are associated with characteristic changes in specific biomarkers, among which the pH of the wound microenvironment is widely regarded as a key physiological parameter reflecting the healing status of the tissue (Alves et al., 2021; Tang et al., 2021). Generally, healthy skin maintains a slightly acidic pH ranging from 4.0 to 6.0. In contrast, chronic wounds often exhibit a mildly alkaline environment (pH > 7.0), with dynamic fluctuations throughout the inflammatory, infectious, and reparative phases (Das & Bal, 2024; Youssef et al., 2023). Therefore, real-time monitoring of wound pH can thus provide reliable insights into the healing stage, infection risk, and treatment response, offering clinicians critical information for timely and personalized interventions (Karthikeyan & Wook Kang, 2025).

At present, a variety of pH-responsive materials have been widely explored for application in intelligent wound dressings, including colorimetric dyes (e.g., phenol red and anthocyanins) (Huang et al., 2024; Zhu et al., 2020), fluorescence-emitting probes (Chai et al., 2023; Zong et al., 2023), and conductive polymers exhibiting pH-dependent electrical changes (e.g., polyaniline and PEDOT: PSS) (Lee et al., 2023;

Mariani et al., 2021). Among them, carbon quantum dots (CQDs), a new class of carbon-based fluorescent nanomaterials, have attracted increasing attention for visual pH monitoring owing to their excellent optical stability, good biocompatibility, and easily functionalizable surface chemistry (Das et al., 2018; Malavika et al., 2022). Polysaccharides have emerged as ideal carbon sources for the green synthesis of biocompatible CQDs due to their abundant availability, structural diversity, and favorable carbonization characteristics (Yao et al., 2024). Starch is a naturally occurring polysaccharide composed of glucose units linked by α-1,4 and α-1,6 glycosidic bonds (Mary et al., 2022). Its high content of hydroxy groups, regular structure, and large surface area make it a promising precursor for preparing CQDs with tunable optical properties and high pH sensitivity (Arias Velasco et al., 2021; Emam, 2024). However, pristine starch suffers from limited solubility and stability, which are unfavorable for forming a uniform and stable carbonization environment (Fu et al., 2019; Miyazaki et al., 2006). In contrast, hydroxypropyl starch (HPS), obtained by substituting hydroxy groups with hydroxypropyl moieties, exhibits enhanced water solubility and structural stability due to weakened internal hydrogen bonding, increased hydrophilicity, and the formation of an expanded three-dimensional network structure, thus providing a more suitable carbon source (Qi et al., 2017). Therefore, synthesizing fluorescent, pH-responsive CQDs from HPS aligns with sustainable material development principles and offers a new route for constructing non-toxic, efficient, and responsive platforms for intelligent wound monitoring.

Previous studies have explored the incorporation of CQDs into hydrogel systems for visual pH monitoring of wounds. For example, Yang et al., (2024) developed a tannic acid/quaternized carboxymethyl chitosan/oxidized sodium alginate@carbon quantum dots hydrogel for monitoring diabetic wounds, while Zheng et al., (2021) co-doped phenol red and CQDs into hydrogels to achieve multimodal pH-responsive sensing. Despite the excellent moisture retention and biocompatibility of hydrogel-based wound dressings, their inherently weak mechanical properties limit their applicability in dynamic wound environments (Shen et al., 2023; Zeng et al., 2022). In contrast, electrospun nanofiber dressings offer superior mechanical flexibility, conformability, breathability, and high surface area, making them more suitable for addressing the dual requirements of functionality and structural integrity in chronic wound management (Liu et al., 2021). Electrospinning, due to its compatibility with diverse polymer systems, precise structural control, and low fabrication cost, has become an ideal technique for constructing nanofibrous wound dressings (Dong et al., 2024). Conventional electrospinning typically employs organic solvents, which pose potential environmental and biosafety concerns; therefore, water-based electrospinning (green electrospinning) has garnered increasing attention (Abrigo et al., 2014; Avossa et al., 2022; Cho et al., 2025). However, such nanofibers often suffer from insufficient water resistance and mechanical strength under hydrated conditions, making crosslinking an effective strategy to enhance their structural stability and functionality (Nauman et al., 2021). Various crosslinking approaches for electrospun nanofibers have been reported, including in situ crosslinking, solution immersion, vapor-phase, and spray-based methods, encompassing both physical and chemical strategies (Han et al., 2023).

Numerous studies have reported electrospun systems based on natural polymers such as collagen, oxidized cellulose, cellulose, and chitosan, which not only capitalize on the advantages of renewable resources but also exhibit excellent biocompatibility and biodegradability (Chen, Tian, et al., 2023; Juncos Bombin et al., 2020). Chitosan, the second most abundant natural linear aminopolysaccharide after cellulose, has been widely used in biomedical applications such as tissue repair and wound dressings due to its excellent biocompatibility, non-toxicity, and enzymatic degradability, and can be electrospun at high fractions using environmentally friendly solvent systems such as aqueous concentrated acetic acid (Aranaz et al., 2021; Ji et al., 2022). Building on this foundation, we introduced acetoacetylated polyvinyl alcohol (AAPVA), a non-toxic, environmentally friendly polymer with

excellent mechanical properties (Liu et al., 2022). Beyond improving processability and biosafety, the acetoacetyl groups in AAPVA impart multifunctional reactivity, enabling the formation of stable covalent crosslinked networks with functional polymers such as chitosan, thereby further enhancing the structural integrity and mechanical strength of the nanofibers under hydrated conditions (Chen, Ma, et al., 2023; Hong et al., 2024). Such a water-based design strategy holds great potential for developing intelligent wound dressings that combine mechanical robustness with functional responsiveness, particularly in terms of wet-state stability and biological safety.

Based on the above background, the objective of this study was to develop a novel pH-responsive electrospun nanofibrous dressing composed of CQDs, CS, and AAPVA. We hypothesized that the abundant polar functional groups on starch-derived CQDs could endow the composite nanofibers with excellent pH sensitivity, while the biocompatible CS would form a stable covalent crosslinked network with AAPVA through Schiff base reactions, thereby enhancing the structural integrity and stability of the nanofibers under moist conditions. Based on this design concept, composite nanofibers were fabricated using an aqueous green electrospinning method, and their physicochemical properties and biocompatibility were systematically evaluated. Finally, a visual pH detection model was established using RGB image analysis to further verify their potential for intelligent management and remote monitoring of chronic wounds.

2. Materials and methods

2.1. Materials

The hydroxypropyl starch (propylene chlorohydrin compounds: less than 1.0 ppm, a degree of hydroxypropyl substitution of 20.0 %, corresponding to a molar substitution of approximately 0.7 per anhydroglucose unit) was obtained from Matsutani Chemical Industry Co., Ltd. (Itami, Japan). The high molecular weight chitosan (CAS RN: 9012-76-4, 310–375 kDa, 73 % deacetylated) was purchased from Sigma-Aldrich Co. (St. Louis, MO, USA). Ethylenediamine (EDA) was purchased from Fujifilm Wako Pure Chemical Co. (Osaka, Japan). Acetoacetylated polyvinyl alcohol (AAPVA, degree of hydrolysis: 99 %, Mw $\approx$ 44,000 g mol^1, acetoacetyl substitution degree: 5 %) was kindly supplied by The Nippon Synthetic Chemical Industry Co., Ltd. (Tokyo, Japan).

2.2. Synthesis and characterization of CQDs

CQDs were synthesized via a one-step hydrothermal method. Specifically, 3 g of starch was gelatinized in 16 mL of deionized water at 90 °C under magnetic stirring for 1 h until complete gelatinization occurred. After complete dissolution, the mixed solution was transferred into a Teflon-lined autoclave, adding 4 mL of ethylenediamine with thorough mixing. The reaction was conducted at 200 °C for 6 h, during which the polysaccharide chains underwent hydrolysis and ring-opening reactions to generate reactive aldehyde intermediates. These intermediates further participated in condensation and polymerization reactions, accompanied by partial carbonization. Upon completion, a brownish-yellow colloidal solution was obtained. The mixture was centrifuged at 12,000 rpm to remove large particulate impurities, and the supernatant was further filtered through a 0.22 μm microporous membrane. The resulting filtrate was subjected to dialysis against 1000 mL of deionized water for 3 days using a dialysis bag (molecular weight cutoff is 1 kDa) to remove small molecular impurities. The solution was freeze-dried at −40 °C under a vacuum pressure of 10 MPa to yield a light-yellow solid powder as the final CQD product. The powder was then stored under controlled conditions at 25 °C and 40 % relative humidity until further use.

2.3. Synthesis and characterization of CQD/CS/AAPVA nanofiber system

Preliminary experiments were conducted to optimize the electrospinning precursor composition. AAPVA solutions at 5 %, 10 %, and 15 % (w/v) were first evaluated under electrospinning conditions. Subsequently, CQDs were incorporated into 10 % (w/v) AAPVA solutions at concentrations of 0 %, 0.5 % and 1 % (w/v). For CS incorporation, 0 %, 0.5 % and 1 % (w/v) CS solutions prepared in 2 % (v/v) acetic acid were blended with the CQDs/AAPVA solution, and different mixing ratios (90:10, 80:20, and 70:30, v/v) were investigated. Based on the optimized parameters, a homogeneous precursor solution containing 10 % (w/v) AAPVA and 1 % (w/v) CQDs was prepared in deionized water at 90 °C under magnetic stirring for 6 h. Separately, a 1 % (w/v) CS solution was prepared in 2 % (v/v) acetic acid, ultrasonicated at room temperature for 1 h, and mixed with the CQDs/AAPVA solution at a volume ratio of 80:20 under magnetic stirring at room temperature for 10 min to obtain the electrospinning blend. Electrospinning was carried out at 25 °C and 45 % relative humidity using a syringe with a 0.8 mm diameter needle, a flow rate of 0.5 mL/h, an applied voltage of 20 kV, and a tip-to-collector distance of 10 cm. Four types of nanofibrous scaffolds were fabricated according to this procedure: (I) AAPVA, (II) CQDs/AAPVA, (III) CS/AAPVA, and (IV) CQDs/CS/AAPVA.

2.4. General characterization

2.4.1. Transmission electron microscope (TEM)

The morphology of the CQDs was characterized using transmission electron microscopy (TEM, JEM-2100, JEOL Ltd., Tokyo, Japan) operated at an acceleration voltage of 200 kV. For observation, a drop of 0.2 wt% CQD dispersion was deposited onto a high-resolution carbon film and subsequently dried under vacuum. The average nanoparticle sizes were determined from the TEM images using ImageJ software.

2.5. Atomic force microscope (AFM)

The height of the CQDs was measured using atomic force microscopy (AFM, SPI3800N/SPA-400, Seiko Instruments Inc., Tokyo, Japan) after depositing a 0.2 wt% CQD aqueous dispersion onto a freshly cleaved mica surface and allowing it to air-dry.

2.5.1. Dynamic light scattering

The hydrodynamic diameter of the CQDs was measured using a particle size analyzer (ELSZ-2000 Series, Otsuka Electronics Co. Ltd., Osaka, Japan). The analysis was performed on a 0.2 wt% CQD aqueous dispersion at room temperature, and the reported values were obtained as the average of three independent measurements to ensure reproducibility.

2.5.2. X-ray diffraction (XRD) and X-ray photoelectron spectroscopy (XPS)

The chemical composition and structural characteristics of the CQDs and electrospun nanofiber membranes were analyzed using X-ray diffraction (XRD, SmartLab, Rigaku Co. Ltd., Tokyo, Japan) and X-ray photoelectron spectroscopy (XPS, KRATOS ULTRA2, Shimadzu Co. Ltd., Kyoto, Japan). For the XRD measurements, patterns were acquired using Cu Kα radiation (λ = 1.54 Å) with an operating voltage of 45 kV and a current of 200 mA, and the diffraction data were normalized prior to analysis. For the XPS measurements, spectra were collected with monochromatic Al Kα radiation (1486.6 eV), and the binding energies were calibrated by referencing the C 1 s peak at 284.6 eV to correct for surface charging effects.

2.5.3. Fourier- transform infrared (FT-IR) spectroscopy

FT-IR spectroscopy measurements of the materials in the 500–4000 cm^{-1} wavenumber range were carried out with a Nicolet iS5 FTIR spectrometer (Thermo Fisher Scientific, Waltham, USA). The spectra were acquired in attenuated total reflectance (ATR) mode using a diamond crystal. The spectra were recorded with a resolution of 4 cm^{-1}, and for each sample, 20 scans were co-added to improve the signal-to-noise ratio. The spectra were baseline-corrected and normalized before analysis.

2.5.4. Ultraviolet–visible (UV–Vis) spectrophotometry

UV–Vis absorption spectra of the CQDs were recorded using a UV–Vis spectrophotometer (U-2810, Hitachi Ltd., Tokyo, Japan) in the wavelength range of 200–800 nm.

2.5.5. Fluorescence (FL) spectroscopy

A microplate reader (SH-9000Lab, Yamato Scientific Co. Ltd., Tokyo, Japan) was used to analyze the photoluminescence (PL) spectra, 3D fluorescence contour map and Commission Internationale de L'Eclairage (CIE) coordinate of the CQDs.

2.5.6. Scanning electron microscopy (SEM)

The nanofibers were mounted on aluminum stubs and sputter-coated with a 20 nm gold–palladium layer before morphological and diameter observation using a scanning electron microscope (Quattro S, Thermo Fisher Scientific, Waltham, USA) operated at an acceleration voltage of 10 kV and equipped with a field emission gun (FEG).

2.5.7. Water contact angle

The water contact angle of the nanofibers was measured at 25 °C using a contact angle goniometer (Drop Master DM300, Kyowa Interface Science Co., Ltd., Saitama, Japan) by applying a 0.5 μL droplet of deionized water onto the nanofibers.

2.5.8. Mechanical properties

Mechanical properties were evaluated using a universal testing machine (EZ Graph, Shimadzu Co., Kyoto, Japan) equipped with a 10 N load cell at a strain rate of 20 mm/min, under conditions of 25 °C and 40 % relative humidity, with sample dimensions of 5 × 20 mm.

2.6. Swelling ratio

Dried samples were weighed and immersed in 10 mL of phosphate-buffered saline (PBS, pH 7.4) at 37 °C to evaluate the swelling ratio (SR). At predetermined time intervals, the samples were carefully removed, excess surface liquid was gently blotted using filter paper, and the swollen samples were weighed. The swelling ratio was calculated using the following equation (Wang et al., 2023):

$$SR = \frac{W_{ss} - W_{ds}}{W_{ds}} \times 100 \tag{1}$$

where W_{ds} and W_{ss} represent the sample weights before and after swelling, respectively. Each experiment was conducted in triplicate.

2.7. In vitro degradation

Nanofibrous membranes with equal initial weights were immersed in 10 mL of PBS solution (pH 7.4) at 37 °C. After 5 days, the samples were removed, rinsed with distilled water, and dried. The weight retention (WR) of the membranes was calculated using the following equation (Dainiak et al., 2010):

$$WR = \frac{W_m - W_n}{W_n} \times 100 \tag{2}$$

where W_n and W_m represent the sample weights before and after degradation, respectively. Each experiment was conducted in triplicate.
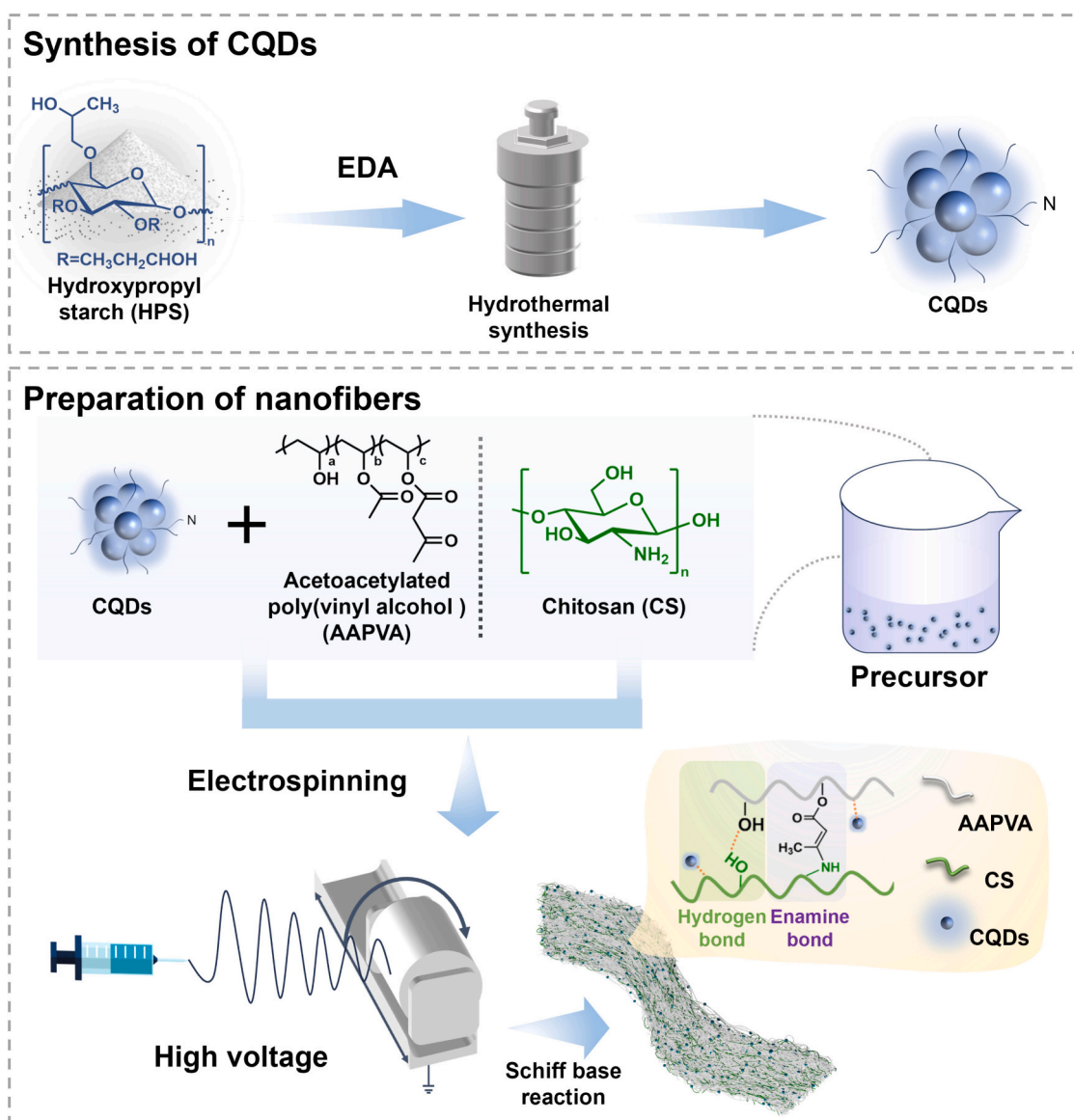
Fig. 1. Schematic of the preparation procedure of CQDs and electrospun nanofibers.

2.8. Morphological stability

To assess the morphological stability during in vitro degradation, samples were immersed in 10 mL of PBS buffer (pH 7.4) at 37 °C and retrieved after 1, 3, and 5 days. After rinsing with distilled water, samples were immediately frozen in liquid nitrogen and subsequently freeze-dried at −40 °C under 10 MPa. The surface morphology of the freeze-dried samples was examined using scanning electron microscopy (SEM, SU5000, Hitachi High-Tech Science Co., Japan). Before observation, the samples underwent gold sputtering on the MSP-1S magnetron sputter and were imaged using a Schottky field-emission electron gun.

2.9. pH-responsive testing of CQDs/CS/AAPVA nanofibers

The color changes of CQDs/CS/AAPVA nanofibers in buffer solutions with different pH values were investigated. Rectangular nanofiber samples (1 × 2 cm) were prepared and immersed in buffer solutions with pH values of 5.0, 5.5, 6.0, 6.5, 7.0, 7.5, and 8.0 at 37 °C for 30 s. After exposure, the color-changed nanofibers were photographed using a smartphone camera. The images were then processed using the free

image analysis software FCPicker to extract the corresponding RGB values. To minimize discrepancies caused by variations in ambient lighting between the captured image and the actual color of the sample, each measurement was repeated three times.

2.10. Biocompatibility: In vitro MEM elution cytotoxicity

According to the recommendations of ISO-10993 standards, cell viability was evaluated via an indirect assay (Liu et al., 2018). The extraction media were prepared by incubating pieces of the electrospun scaffolds (6 cm^2/ml) in cell culture medium at 37 °C for three days. Each scaffold piece with an area of 6 cm^2 (≈0.36 g) contained about 2.9 mg of CQDs. L929 fibroblast cells were seeded at a concentration of 3000 cells/well into 96-well plates and cultured with DMEM (Gibco, United States), 10 % Fetal calf serum (FSC, Gibco, United States), 1 % Penicillin-Streptomycin/Amphotericin B Mix (PanBiotech, Germany) for 24 h. Subsequently, the culture medium was removed and replaced with extraction media, and the cells were further incubated for another 24 h. Normal medium was used as the negative control, while medium containing 10 % DMSO (Sigma-Aldrich, United States) was the positive control. Five wells were tested for each material (*n* = 5). Cell metabolic
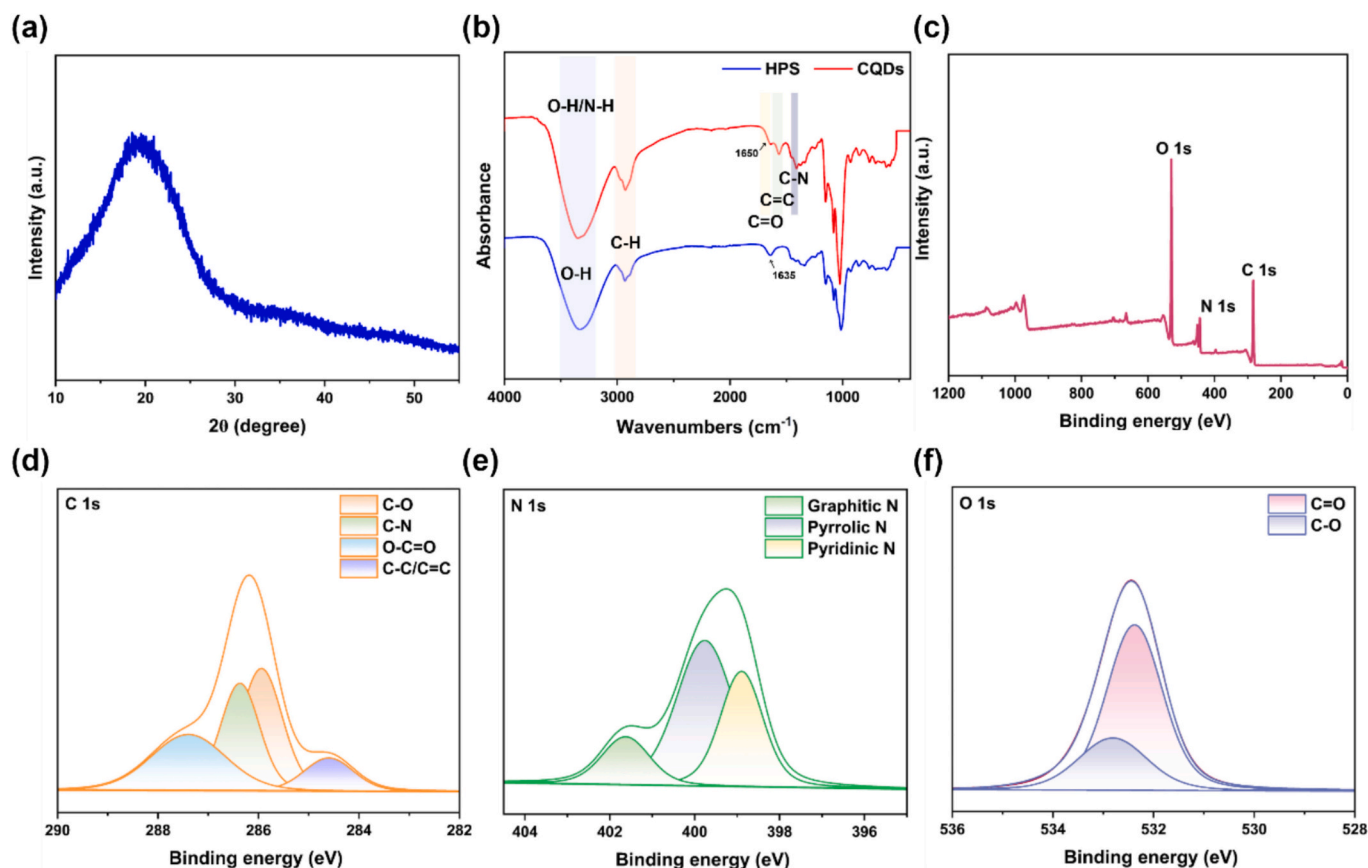
Fig. 2. (a) XRD patterns of CQDs; (b) FTIR spectra of HPS and CQDs; (c) full-scan XPS spectra, (d) C 1 s, (e) N 1 s, and (f) O 1 s XPS spectra of the prepared CQDs.

activity after exposure to different extract media was assessed using the CellTiter-Blue® Cell Viability Assay (Promega, Germany). To evaluate cell morphology, fluorescence imaging (Nikon, Japan) was performed using Phalloidin-iFluor™ 488 (Cayman Chemicals, United States) and DAPI (Carl ROTH, Germany) for nuclear staining, allowing visualization of cell morphology and viability.

2.11. Statistical analysis

All experimental data from three or more independent experiments are expressed as mean ± standard deviation. One-way ANOVA was used to estimate all data. ($****\ p < 0.0001$, $***\ p < 0.001$, $**\ p < 0.01$, $*\ p < 0.05$).

3. Results and discussion

3.1. Synthesis and characterization of CQDs

The synthesis process of CQDs using HPS as the carbon precursor and ethylenediamine as the nitrogen source via a one-pot hydrothermal method is illustrated in Fig. 1. TEM and AFM images revealed that the resulting CQDs were quasi-spherical nanoparticles with an average diameter of 2.39 ± 0.64 nm (Fig. S2a, S2b and S2c). XRD pattern of the synthesized CQDs (Fig. 2a) displayed a broad diffraction peak centered around $2\theta \approx 20°$, which is larger than the (002) interlayer spacing of graphite, indicating a highly disordered (amorphous) carbon structure. This is likely attributed to the abundance of oxygen-containing surface groups (Liu, Yu, et al., 2025).

The chemical structure of the CQDs was characterized by FT-IR and XPS. As shown in Fig. 2b, new absorption bands emerged at $\sim1650\ cm^{-1}$ and $1560\ cm^{-1}$ in the CQD spectrum, corresponding to C=O and C=C stretching vibrations, respectively (Preethi et al., 2022; Sun et al., 2024).

A peak at $1405\ cm^{-1}$ was assigned to C—N stretching, confirming the introduction of nitrogen-related groups (Sharma et al., 2020). The full survey spectrum (Fig. 2c) shows characteristic peaks at binding energies of 284.0, 399.0, and 532.0 eV, corresponding to C 1 s, N 1 s, and O 1 s, respectively. This successful nitrogen doping is expected to enrich the surface states of the CQD framework, thereby enhancing their photoluminescent properties. As shown in the high-resolution C 1 s spectrum (Fig. 2d), four peaks were observed at 284.60, 285.94, 286.37, and 287.39 eV, corresponding to C–C/C=C, C—O, C—N, and C=O, respectively. The N 1 s spectrum (Fig. 2e) revealed three nitrogen configurations: pyridinic N (398.90 eV), pyrrolic N (399.76 eV), and graphitic N (401.63 eV). In the O 1 s spectrum (Fig. 2f), two peaks at 532.38 and 533.81 eV were attributed to C=O and C—O, respectively. These results collectively confirm the functional groups identified by FTIR and demonstrate the successful incorporation of nitrogen atoms into the CQD structure. (Lohrasbi Nejad & Shekarchizadeh, 2024; Pallavolu et al., 2023). The presence of these functional groups ensures excellent dispersibility of the CQDs in aqueous media. The average hydrodynamic diameter of the CQD aqueous suspension was 4.3 nm, slightly larger than the TEM-measured size (Fig. S2d).

3.2. Fluorescence properties of CQDs

The photophysical properties of the CQDs are presented in Fig. 3. As shown in Fig. 3a, the CQD aqueous solution appeared transparent under daylight (DL), while a distinct cyan–blue fluorescence was observed under 365 nm ultraviolet (UV) light irradiation. The UV–vis absorption spectrum (Fig. 3b) displayed three characteristic peaks. A broad absorption band centered at 230 nm is attributed to the π–π* transitions of C=C bonds within the sp²-hybridized carbon core. A shoulder peak around 283 nm corresponds to n–π* transitions associated with oxygen-
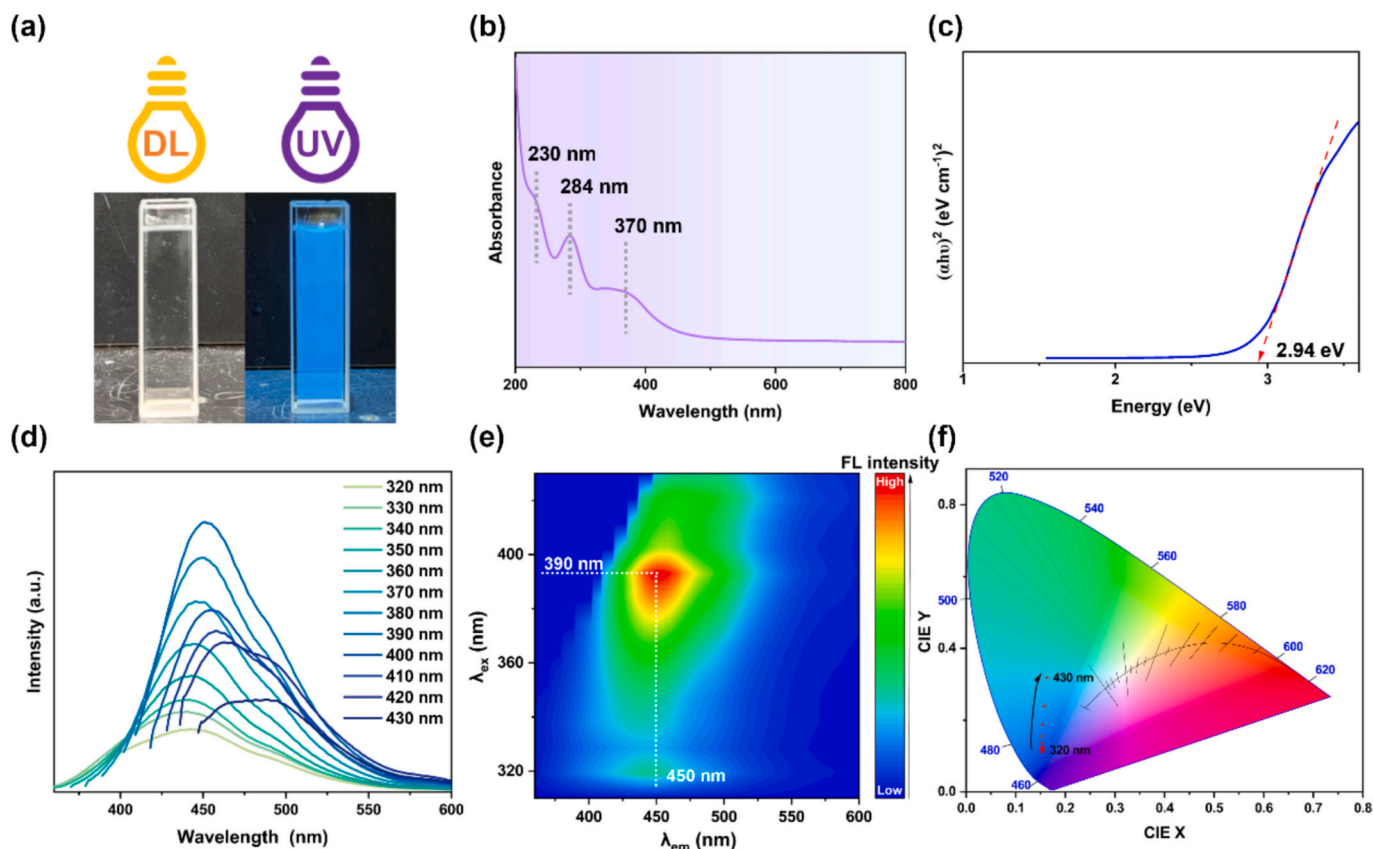
Fig. 3. (a) digital photographs of CQDs solutions under visible and UV light excitation; (b) UV–vis absorption spectra of CQDs; (c) Tauc plots of CQDs; (d) Excitation-dependent PL spectra of CQDs; (e) Three-dimensional fluorescence mapping of CQDs; (f) CIE coordinate of CQDs.

containing surface functional groups on sp^3-hybridized carbon. Additionally, a weak shoulder at approximately 370 nm is ascribed to heteroatom-doped surface states or energy traps arising from the n–π* transitions of surface functional groups (Ahmad Farid et al., 2024). These absorption features indicate the coexistence of conjugated carbon domains and oxygenated functional groups on the CQD surface (Ateia et al., 2024). The optical band gap (Eg) of the CQDs was estimated from the Tauc plot (Fig. 3c) using the following equation (Tauc et al., 1966):

$$(\alpha h\nu)^2 = A(h\nu - E_g) \tag{3}$$

where α is the normalized absorption coefficient, hν is the photon energy, and E_g represents the optical band gap. By extrapolating the linear portion of the Tauc curve, the direct band gap of the CQDs was determined to be approximately 2.94 eV. This band gap value is consistent with the cyan–blue fluorescence emission observed under 365 nm excitation, indicating that the electrons in the CQDs can be readily excited to the conduction band, resulting in strong photoluminescence even under low-energy excitation (Ahmad Farid et al., 2024). The band gap of CQDs is highly dependent on their core carbon structure, surface states, and heteroatom doping.

Photoluminescence provides a non-invasive optical readout, making it directly relevant for real-time detection of physiological changes such as wound pH, which is a key biomarker of healing progression and infection risk. To further investigate the PL properties, fluorescence emission spectra under different excitation wavelengths were recorded (Fig. 3d). The emission peak was most intense at 450 nm when excited at 390 nm. As the excitation wavelength increased from 320 to 430 nm, a progressive red shift of the emission peak was observed, indicating a typical excitation-dependent behavior, which suggests the involvement of multiple emissive energy states or surface defect states in the PL process. Based on this, a 3D fluorescence contour map (Fig. 3e) was

obtained, which confirmed the optimal excitation and emission wavelengths of 390 nm and 450 nm, respectively. Additionally, the color evolution of the emitted light under different excitation wavelengths was analyzed using the CIE coordinate (Fig. 3f). The emission color gradually shifted from blue to cyan blue as the excitation wavelength increased from 320 to 430 nm, confirming the excitation-dependent fluorescence behavior.

To evaluate the photostability of the CQDs, their fluorescence was monitored under continuous UV irradiation in both aqueous and PBS solutions (Fig. S3a and S3b). Although a gradual decrease in intensity was observed over time, the CQDs retained more than 85 % of their initial fluorescence after 3 h of irradiation, demonstrating sufficient stability for practical use. Furthermore, the photoluminescence response of freshly prepared samples and those stored for six months under ambient conditions showed no obvious difference under 365 nm excitation, confirming the long-term stability of the synthesized CQDs (Fig. S3c). These results demonstrate that the synthesized CQDs possess moderate band gap energy, pronounced excitation-dependent fluorescence, and excellent photostability, providing a robust functional basis for their application in pH-responsive, visually trackable wound dressings for real-time monitoring of the healing process.

3.3. Fabrication and characterization of nanofibers

To address the issue of secondary tissue damage caused by repeated infections and frequent dressing changes, and to facilitate wound healing alongside real-time monitoring and auxiliary treatment, a smart-responsive CQDs/CS/AAPVA composite nanofiber dressing was fabricated via electrospinning. In preliminary optimization, 10 % (*w/v*) AAPVA was identified as the most suitable concentration, as lower or higher concentrations resulted in bead formation or unstable jetting
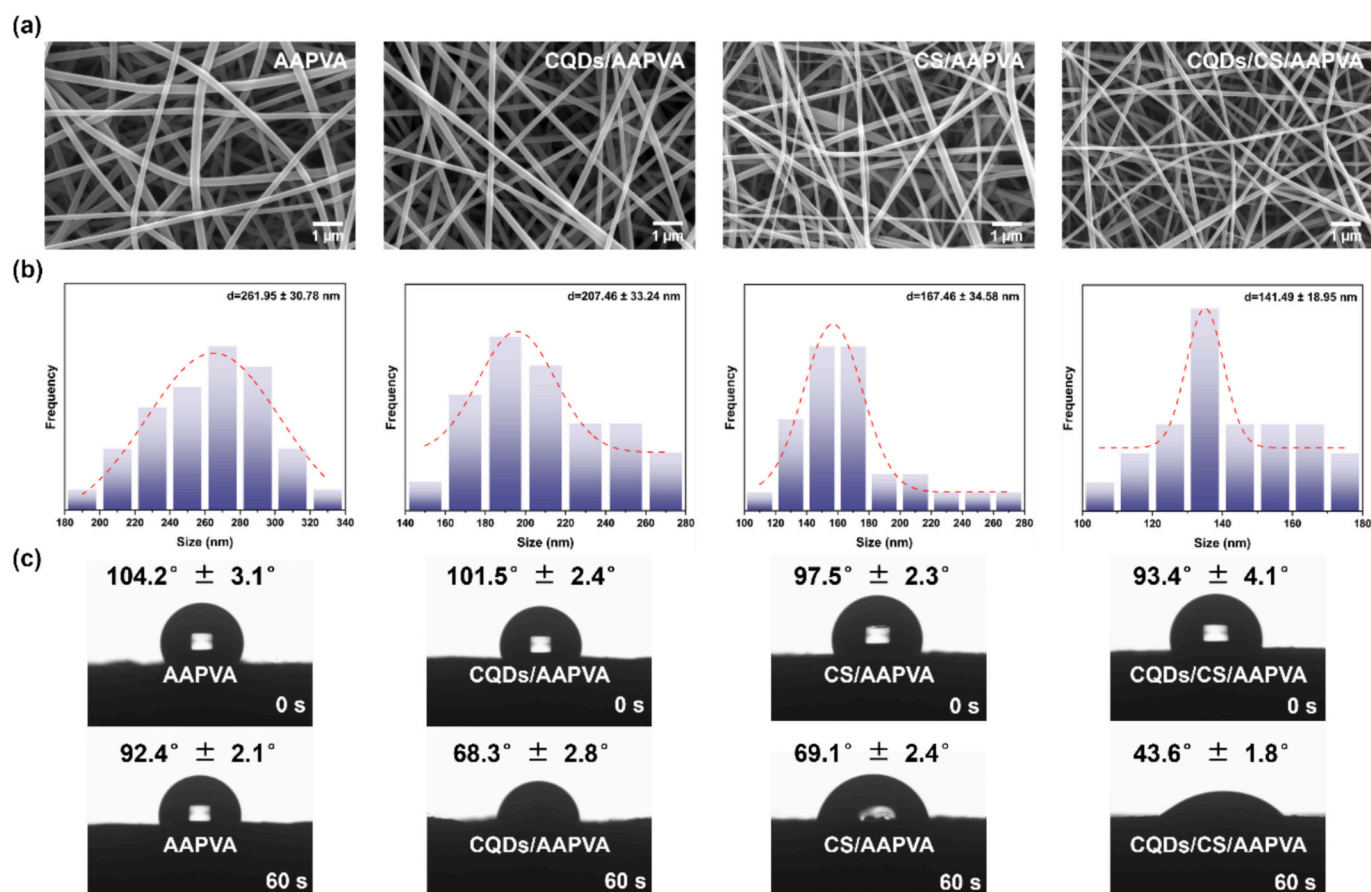
Fig. 4. (a) SEM micrographs, (b) diameter distribution, and (c) water contact angles (0 and 60 s) of AAPVA, CQDs/AAPVA, CS/AAPVA, and CQDs/CS/AAPVA nanofibers.

(Fig. S4). For CQDs loading, 1 % (w/v) provided uniform and strong fluorescence under UV illumination, whereas 0.5 % (w/v) produced weak and uneven signals (Fig. S5). With respect to the CS fraction, the 80:20 (CQDs/ AAPVA:CS) mixing ratio offered a balance between viscosity, conductivity, and spinnability, leading to uniform fibers with minimal defects (Fig. S6). Attempts to electrospin CS/CQDs alone under comparable conditions failed to yield continuous fibers, likely due to insufficient entanglement and high conductivity. These optimized conditions were therefore adopted for subsequent scaffold fabrication. The surface morphology and fiber diameter distribution were analyzed by SEM (Fig. 4a and b). The results revealed a progressive reduction in fiber diameter across the four groups: AAPVA (261.95 ± 30.78 nm), CQDs/ AAPVA (207.46 ± 33.24 nm), CS/AAPVA (167.46 ± 34.58 nm), and CQDs/CS/AAPVA (141.49 ± 18.95 nm). Incorporating polar functional groups from both CQDs and chitosan significantly increased the conductivity of the electrospinning solution, thereby enhancing the electrostatic stretching effect under high voltage conditions (Ju et al., 2025). This improvement facilitated the formation of thinner nanofibers and a denser, more uniform fiber network in the CQDs/CS/AAPVA group. Therefore, the fiber diameter gradually decreased, which is consistent with the statistical analysis (Table S1). The wettability of the nanofiber dressings was evaluated by static water contact angle measurements (Fig. 4c). A water droplet was placed on the fiber surface, and the contact angle was recorded at 0 s and 60 s. Due to the abundance of hydrophilic hydroxy groups on the fiber surface, the water contact angle rapidly decreased within a short period, demonstrating pronounced hydrophilicity (Madani et al., 2025). This behavior is advantageous for the rapid absorption of wound exudates and supports the establishment of a moist environment conducive to wound healing.

The chemical structure of the nanofibers was further explored by FT-IR (Fig. 5a). In the spectra of CS/AAPVA and CQDs/CS/AAPVA composite nanofibers, a clear shift was observed in the characteristic stretching vibration band of the acetoacetyl $C=O$ group (1700–1730 cm^{-1}), along with the emergence of new absorption peaks at ~1650 and ~1605 cm^{-1}, representing the formation of enamine bonds (Rong et al., 2019). These results indicate the occurrence of Schiff base reactions between the amino groups of CS and the acetoacetyl groups of AAPVA. Moreover, the interaction between CQDs and AAPVA can be assigned to hydrogen bonding, which helps immobilize CQDs on the AAPVA chains, evidenced by a shift of the –OH bending vibration peak from 1420 cm^{-1} to around 1408 cm^{-1}. In addition, the observed blue shift of the –OH vibration band further indicates the presence of hydrogen-bonding interactions among AAPVA, CQDs, and CS, suggesting that both chemical and physical interactions contribute to the stability and structural modulation of the composite nanofibers. The crystalline structures of CS, AAPVA, CQDs/AAPVA, CS/AAPVA, and CQDs/CS/AAPVA nanofibers were characterized by XRD (Fig. S7). All samples exhibited broad diffraction humps centered around $2\theta \approx 20°$, with no sharp crystalline peaks observed, indicating predominantly amorphous structures. This amorphous nature mainly originates from the AAPVA matrix, and importantly, the incorporation of CQDs and CS into the electrospinning solution prior to fiber formation did not disrupt the amorphous nature or the uniform morphology of the resulting nanofibers. Amorphous materials typically possess good flexibility and film-forming ability, which are advantageous for producing uniform, dense, and functionally integrated nanofiber dressings, particularly suitable for flexible and conformable wound care applications.

Representative stress-strain curves for nanofiber dressings are shown in Fig. 5b and Table S1. The incorporation of chitosan significantly improved the mechanical performance by forming chemical crosslinks
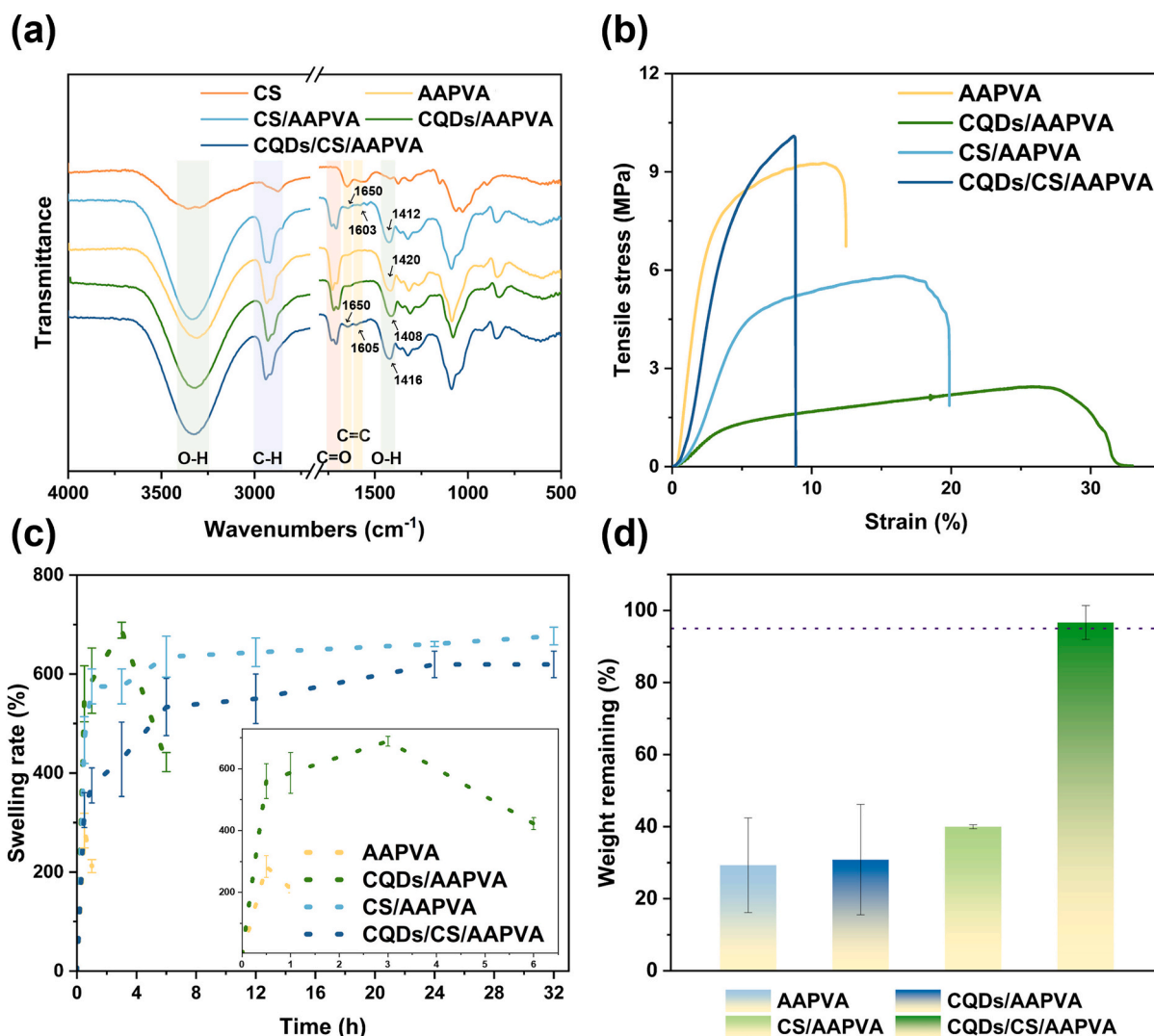
Fig. 5. (a) FT-IR of CS powder, AAPVA, CS/AAPVA, CQDs/AAPVA and CQDs/CS/AAPVA nanofibers; (b) the stress-strain curve, (c) the swelling rate, and (d) in vitro degradation properties in PBS solution (pH = 7.4) within 5 days of AAPVA, CS/AAPVA, CQDs/AAPVA and CQDs/CS/AAPVA nanofibers.

through Schiff base reactions with AAPVA. This chemical interaction enhanced inter-chain connectivity, enabling the material to maintain sufficient strength while exhibiting improved ductility. Furthermore, although incorporating CQDs slightly reduced the ultimate tensile strength, it notably enhanced the flexibility and toughness of the nanofibers. This enhancement is likely attributed to forming a flexible hydrogen-bonded network between CQDs and polymer chains. Comparative analysis of the mechanical properties of CS/AAPVA and CQDs/AAPVA nanofibers revealed a synergistic effect between CQDs and CS, further improving the tensile performance. The resulting CQDs/CS/AAPVA composite nanofibers exhibited a maximum tensile strength of approximately 10 MPa, along with adequate flexibility, indicating excellent overall mechanical performance. Such flexibility and strength are particularly beneficial for enabling close conformity of the dressing to wounds on various anatomical surfaces, thus improving clinical applicability.

Fig. 5c illustrates the swelling behavior of the nanofiber materials in pH 7.4 PBS buffer. AAPVA and CQDs/AAPVA fibers exhibited structural collapse within 2 h and 6 h, preventing further quantitative measurement of swelling. In contrast, CS/AAPVA and CQDs/CS/AAPVA fibers displayed a multi-stage swelling profile with apparent plateaus at ~2, 4, 6, and 24 h, reaching 676.9 ± 17.8 % and 619.4 ± 26.8 % at 24 h while maintaining fibrous integrity. FTIR spectra of CS/AAPVA and CQDs/CS/

AAPVA after 24 h revealed a blue shift of the O—H band, indicating new hydrogen bond formation, which together with the more stable enamine linkages contributed to progressive network densification (Fig. S8). To further evaluate in vitro degradation behavior, the mass loss of nanofibers after 5 days of immersion in PBS (pH = 7.4) was measured, as shown in Fig. 5d. Only the CQDs/CS/AAPVA sample exhibited a mass loss below 5 %, suggesting that the synergistic interaction between CQDs and CS with AAPVA generated a denser and more stable nanofiber network. In contrast, the other samples underwent pronounced disintegration, leaving only large fragments as residual mass. This stability was further confirmed by SEM analysis (Fig. S9), which revealed distinct morphological evolution at 1, 3, and 5 days. Specifically, AAPVA and CQDs/AAPVA gradually lost their fibrous morphology due to swelling, network expansion, and collapse, while CS/AAPVA and especially CQDs/CS/AAPVA largely preserved their fibrous structure even after 24 h, consistent with swelling results. The superior stability of CQDs/CS/ AAPVA is attributed to both the chemical crosslinking between CS and AAPVA and the additional physical interactions introduced by CQDs, which synergistically enhance crosslinking density and suppress fiber merging. Additionally, the thermal stability of the nanofibers was assessed using thermogravimetric analysis (TGA) (Fig. S10). All nanofiber samples exhibited initial decomposition temperatures above 200 °C, indicating satisfactory thermal resistance suitable for
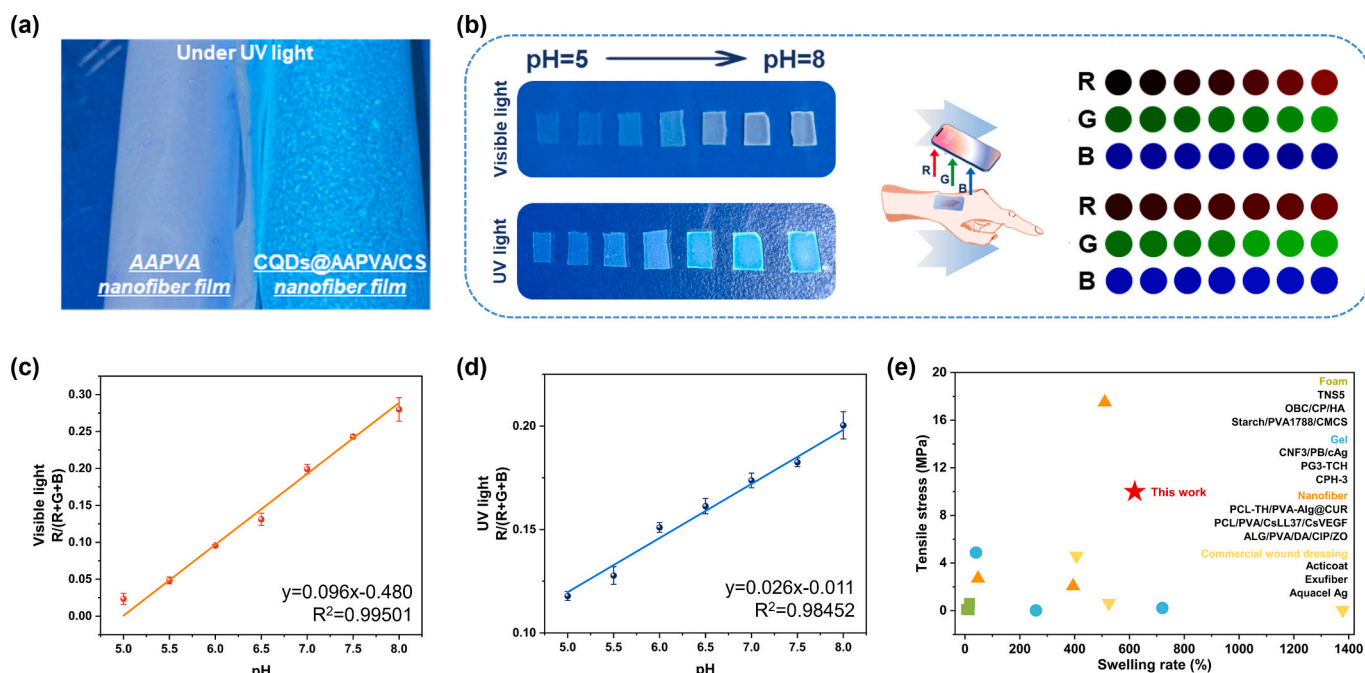
Fig. 6. (a) Digital photographs of AAPVA and CQDs/CS/AAPVA nanofibers under UV light; (b) Photographs and RGB images of CQDs/CS/AAPVA nanofibers with pH values ranging from 5 to 8 under UV and visible light; RGB values and fitted curves of CQDs/CS/AAPVA nanofibers as a function of pH under (c) visible light and (d) UV light. Data are presented as mean ± SD ($n = 3$); (e) Comparison of the developed CQDs/CS/AAPVA nanofiber dressing with existing smart and passive wound dressings, including PVA-based foams (Hou et al., 2025; Liu, Cao, et al., 2025; Liu, Hu, et al., 2025), gels (Ding et al., 2025; Zhang et al., 2025; Zhu et al., 2025), and nanofibers (Cao et al., 2024; Fahimirad et al., 2024; Sadeghi-Aghbash et al., 2024), as well as several commercially available dressings (Minsart et al., 2022).

biomedical applications. The major degradation peaks were observed at ~365 °C for AAPVA, ~345 °C for CQDs/AAPVA, ~358 °C for CS/AAPVA, and ~ 352 °C for CQDs/CS/AAPVA. The lower degradation temperature of CQDs/AAPVA indicates that the interaction between CQDs and AAPVA is mainly physical, providing interfacial contact but limited thermal reinforcement. In contrast, the incorporation of CS introduced partial crosslinking with AAPVA, which slightly stabilized the structure and shifted the degradation peak upward. Overall, the addition of CQDs or CS caused only minor variations, suggesting that the overall thermal stability of the composite nanofibers remained largely unchanged.

3.4. pH responsiveness of CQDs/CS/AAPVA nanofibers

The pH-responsive fluorescence behavior of CQDs is of great importance for their application in wound monitoring. To evaluate this property, the optical response of CQDs in aqueous solutions with pH values ranging from 5 to 8 was investigated (Fig. S11a). In dispersion, the fluorescence intensity of CQDs significantly decreased with increasing pH from 5 to 8 (Fig. S11b and S11c), which can be attributed to the deprotonation of surface functional groups. To translate this intrinsic behavior into a practical dressing system, CQDs were further embedded into the nanofiber matrix.

A pH-responsive CQDs/CS/AAPVA nanofiber dressing was developed, in which CQDs were uniformly distributed throughout the matrix, ensuring stable fluorescence and making the system suitable for chronic wounds with moderate and persistent exudation (Fig. 6a and Fig. S12). This platform enables dual-mode pH visualization under both visible and UV light (Fig. 6b). Visually, the dressing transitioned from translucent to opaque white with increasing pH, providing a clear visual cue of pH changes. Under UV light, the fluorescence color shifted from pale blue to cyan, enhancing the visual contrast of the fluorescent response. In contrast to the dispersion behavior, embedding CQDs within the CS/AAPVA nanofiber matrix led to an overall increase in fluorescence intensity under UV light with rising pH. Such a reversed trend is not due to

the intrinsic response of CQDs themselves but results from pH-induced structural rearrangements in the nanofiber matrix, which enhance light scattering, decrease transparency, and thereby amplify the apparent fluorescence signal (Cimadoro et al., 2018; Wang et al., 2022). Considering that most human-perceived colors can be quantified using the RGB color model, an image-based pH sensing system was proposed using smartphone-assisted acquisition and RGB extraction to represent wound pH digitally. Fig. 6c and d show strong linear correlations between pH values and corresponding RGB intensities under visible and UV light. Accordingly, pH estimation equations were constructed under visible (Eq. 4) and UV illumination (Eq. 5).

$$pH = 4.99 + \frac{R}{0.096(R + G + B)} \tag{4}$$

$$pH = 0.42 + \frac{R}{0.026(R + G + B)} \tag{5}$$

The fluorescence stability of CQDs/CS/AAPVA nanofibers was further examined under different pH and moist conditions (Fig. S13). When alternately immersed in pH 5 and pH 8 buffers for three consecutive cycles, the recorded fluorescence intensities within the same buffer exhibited negligible variation, indicating excellent reversibility. In addition, the nanofibers were immersed in PBS buffer (pH 7.4) for five days, and no noticeable change in fluorescence intensity was observed by naked eye, suggesting that the optical response remained stable under prolonged moist environments. These findings highlight the practical relevance of PL in CQDs-based nanofibers, as they enable a dual-mode, smartphone-assisted sensing platform for intelligent wound management, where fluorescence serves as a visual indicator of wound status.

To further contextualize the practical relevance of the developed nanofiber dressing, a comparison was made with existing smart and passive wound dressings, including PVA-based foams, gels, and nanofibers, as well as several commercially available dressings (Fig. 6e). The results demonstrate that while reported foams and gels exhibit high
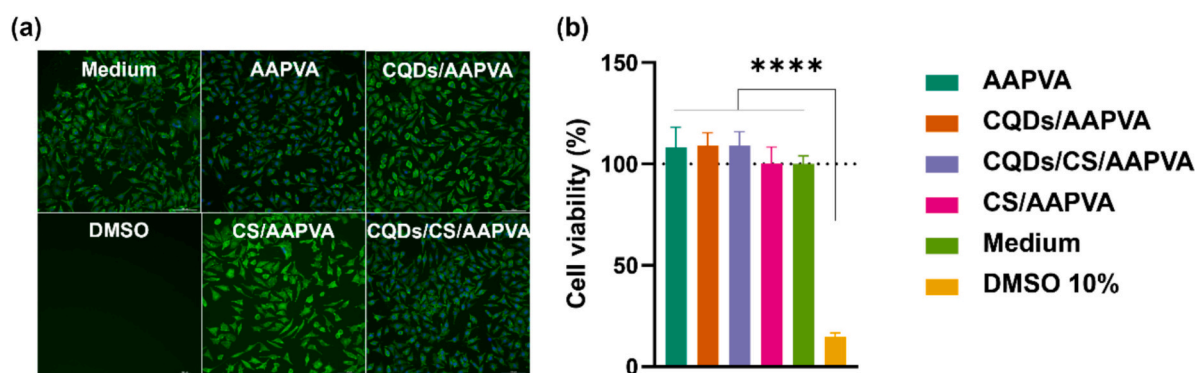
Fig. 7. In vitro cytocompatibility assessment of nanofibers. (a) Fluorescence microscopy images and (b) cell viability of L929 cells cultivated with AAPVA, CS/AAPVA, CQDs/AAPVA, and CQDs/CS/AAPVA nanofibers (**** $p < 0.0001$).

swelling ratios, they generally suffer from poor mechanical strength, which limits their structural integrity under moist wound conditions. In contrast, nanofiber systems provide better mechanical stability but usually compromise on fluid uptake. The present CQDs/CS/AAPVA nanofiber dressing effectively combines these advantages, exhibiting both a significantly higher swelling ratio than typical nanofiber dressings and a markedly improved tensile strength compared to hydrogels and foams. Although its swelling ratio may not surpass that of some hydrogel- or foam-based systems, the overall balance between fluid absorption and mechanical robustness highlights the material's comprehensive performance. Compared with commercial dressings, it provides a more balanced performance between fluid management and mechanical robustness, underscoring its potential for chronic wound care.

3.5. Cell viability of nanofibers

Cytotoxicity evaluation is critical for assessing the suitability of wound dressings in clinical wound management. This study assessed the cytocompatibility of AAPVA, CQDs/AAPVA, CS/AAPVA, and CQDs/CS/AAPVA nanofibers using ISO 10993 standards. As shown in the fluorescence microscopy images (Fig. 7a), L929 fibroblasts exhibited morphological features characteristic of active, mature cells, comparable to those cultured in fresh medium, indicating good cytocompatibility. Furthermore, quantitative analysis of cellular metabolic activity (Fig. 7b) demonstrated that the relative viability of fibroblasts cultured with extracts from AAPVA, CQDs/AAPVA, CS/AAPVA, and CQDs/CS/AAPVA nanofibers was 108.4 ± 9.7 %, 109.2 ± 6.2 %, 100.4 ± 8.0 %, and 109.1 ± 6.8 %, respectively. Cell viability in all experimental groups exceeded 100 % relative to the negative control, confirming the excellent cytocompatibility of the developed composite dressings. This enhancement can be attributed to the synergistic biological effects of the three polymeric components. AAPVA contributes to a moist and stable microenvironment due to its hydrophilic nature and reactive acetoacetyl groups, CS promotes cell adhesion and regeneration through its cationic bioactivity, and CQDs are known to stimulate mitochondrial activity and modulate intracellular signaling pathways via their abundant surface functional groups (Azad et al., 2004; El Ghacham et al., 2025; Sung et al., 2010).

4. Conclusion

Nitrogen-doped CQDs were successfully synthesized using starch as a biomass-derived carbon source through a green hydrothermal method. These CQDs were incorporated into an aqueous electrospinning system comprising AAPVA and CS, resulting in a composite nanofibrous dressing with excellent biocompatibility and environmental safety. The fabricated CQDs/CS/AAPVA nanofibers demonstrated strong mechanical properties (tensile strength of 10.0 MPa), high swelling capacity ($\sim 619.4 \pm 26.8$ %), and outstanding structural integrity, retaining clear fibrous morphology after 5 days in PBS (pH 7.4) with a mass loss of less than 5 %. Notably, the dressing exhibited highly visible and reversible optical responses to pH changes within the range of 5–8 under both daylight and UV light. By integrating RGB image analysis via mobile devices, these pH-responsive color and fluorescence changes enabled accurate, non-invasive quantification of wound pH. The developed CQDs/CS/AAPVA nanofibers present a facile, cost-effective, and sustainable strategy for developing innovative wound dressings capable of real-time monitoring and intelligent management of chronic wounds.

CRediT authorship contribution statement

Ying Yao: Writing – original draft, Methodology, Investigation, Formal analysis, Data curation, Conceptualization. **Yu-I Hsu:** Writing – review & editing, Supervision, Funding acquisition, Conceptualization. **Selina Sonntag:** Investigation, Formal analysis. **Alicia Fernández-Colino:** Writing – review & editing. **Stefan Jockenhövel:** Writing – review & editing. **Hiroshi Uyama:** Writing – review & editing, Supervision, Funding acquisition.

Declaration of competing interest

The authors declare that they have no known competing financial interests or personal relationships that could have appeared to influence the work reported in this paper.

Acknowledgments

Appendix A. Supplementary data

Supplementary data to this article can be found online at https://doi.org/10.1016/j.carbpol.2025.124477.

Data availability

Data will be made available on request.

References

Abrigo, M., McArthur, S. L., & Kingshott, P. (2014). Electrospun nanofibers as dressings for chronic wound care: Advances, challenges, and future prospects. *Macromolecular Bioscience, 14*(6), 772–792. https://doi.org/10.1002/mabi.201300561

Ahmad Farid, M. A., Lease, J., & Yoshito, A. (2024). Lignocellulosic biomass-derived carbon quantum dots (CQDs): A novel approach utilizing organosolv lignin from Moso bamboo waste. *Journal of Cleaner Production, 467*, Article 142852. https://doi.org/10.1016/j.jclepro.2024.142852

Alves, P. M., Barrias, C. C., Gomes, P., & Martins, M. C. L. (2021). Smart biomaterial-based systems for intrinsic stimuli-responsive chronic wound management. *Materials Today Chemistry, 22*, Article 100623. https://doi.org/10.1016/j.mtchem.2021.100623

Aranaz, I., Alcántara, A. R., Civera, M. C., Arias, C., Elorza, B., Heras Caballero, A., & Acosta, N. (2021). Chitosan: An overview of its properties and applications. *Polymers, 13*(19), Article 19. https://doi.org/10.3390/polym13193256

Arias Velasco, V., Caicedo Chacón, W. D., Carvajal Soto, A. M., Ayala Valencia, G., Granada Echeverri, J. C., & Agudelo Henao, A. C. (2021). Carbon quantum dots based on carbohydrates as nano sensors for food quality and safety. *Starch - Stärke, 73*(11−12), Article 2100044. https://doi.org/10.1002/star.202100044

Ateia, E. E., Rabie, O., & Mohamed, A. T. (2024). Assessment of the correlation between optical properties and CQD preparation approaches. *The European Physical Journal Plus, 139*(1), Article 24. https://doi.org/10.1140/epjp/s13360-023-04811-7

Avossa, J., Herwig, G., Toncelli, C., Itel, F., & Michel Rossi, R. (2022). Electrospinning based on benign solvents: Current definitions, implications and strategies. *Green Chemistry, 24*(6), 2347–2375. https://doi.org/10.1039/D1GC04252A

Azad, A. K., Sermsintham, N., Chandrkrachang, S., & Stevens, W. F. (2004). Chitosan membrane as a wound-healing dressing: Characterization and clinical application. *Journal of Biomedical Materials Research Part B: Applied Biomaterials, 69B*(2), 216–222. https://doi.org/10.1002/jbm.b.30000

Cao, W., Xia, D., Zhou, L., Liu, Y., Wang, D., Liang, C., & Chen, M. (2024). Antibacterial and antioxidant wound dressings with pH responsive release properties accelerate chronic wound healing. *Materials Today Physics, 40*, Article 101316. https://doi.org/10.1016/j.mtphys.2023.101316

Chai, L., Li, Y., Yang, H., Wang, Y., Huang, R., Wei, Z., & Zhan, Z. (2023). pH-triggered fluorescent probe for sensing of hypochlorite and viscosity in live cells and chronic wound diabetic mice. *Sensors and Actuators B: Chemical, 393*, Article 134345. https://doi.org/10.1016/j.snb.2023.134345

Chen, D., Tan, G., Tian, S., Han, L., Li, Y., Tan, Y., & Chen, K. (2024). Advancements in nanozymes research for the management of chronic wounds. *Chemical Engineering Journal, 500*, Article 157299. https://doi.org/10.1016/j.cej.2024.157299

Chen, S., Tian, H., Mao, J., Ma, F., Zhang, M., Chen, F., & Yang, P. (2023). Preparation and application of chitosan-based medical electrospun nanofibers. *International Journal of Biological Macromolecules, 226*, 410–422. https://doi.org/10.1016/j.ijbiomac.2022.12.056

Chen, X., Ma, Y., Qiao, Y., Guo, W., Min, Y., Fan, J., & Shi, Z. (2023). Strong and tough octyl enamine-grafted polyvinyl alcohol with programmable shape deformation via simple soaking treatment. *Materials Advances, 4*(11), 2457–2465. https://doi.org/10.1039/D3MA00187C

Cho, Y., Baek, J. W., Sagong, M., Ahn, S., Nam, J. S., & Kim, I.-D. (2025). Electrospinning and nanofiber technology: Fundamentals, innovations, and applications. *Advanced Materials, 37*(28), Article 2500162. https://doi.org/10.1002/adma.202500162

Cimadoro, J., Ribba, L., Ledesma, S., & Goyanes, S. (2018). Electrospun Mats: From White to transparent with a drop. *Macromolecular Materials and Engineering, 303*(10), Article 1800237. https://doi.org/10.1002/mame.201800237

Dainiak, M. B., Allan, I. U., Savina, I. N., Cornelio, L., James, E. S., James, S. L., … Galaev, I. Y. (2010). Gelatin–fibrinogen cryogel dermal matrices for wound repair: Preparation, optimisation and *in vitro* study. *Biomaterials, 31*(1), 67–76. https://doi.org/10.1016/j.biomaterials.2009.09.029

Das, I. J., & Bal, T. (2024). pH factors in chronic wound and pH-responsive polysaccharide-based hydrogel dressings. *International Journal of Biological Macromolecules, 279*, Article 135118. https://doi.org/10.1016/j.ijbiomac.2024.135118

Das, R., Bandyopadhyay, R., & Pramanik, P. (2018). Carbon quantum dots from natural resource: A review. *Materials Today Chemistry, 8*, 96–109. https://doi.org/10.1016/j.mtchem.2018.03.003

Ding, L., Qi, Q., Zhang, S., Ren, C., Deng, M., Sun, Z., Zhang, R., Liu, Q., Duan, S., Wang, X., & Wang, L. (2025). Hydroxypropyl methylcellulose reinforced collagen/PVA composite hydrogel wound dressing with self-adaptive, hemostasis and antibacterial ability for wound healing. *International Journal of Biological Macromolecules, 304*, Article 140811. https://doi.org/10.1016/j.ijbiomac.2025.140811

Dong, Y., Fu, S., Yu, J., Li, X., & Ding, B. (2024). Emerging smart Micro/nanofiber-based materials for next-generation wound dressings. *Advanced Functional Materials, 34*(9), Article 2311199. https://doi.org/10.1002/adfm.202311199

El Ghacham, S., Hejji, L., El Hadj, A., Ali, Y., Wahby, A., Tamegart, L., … Azzouz, A. (2025). Enhanced antibacterial and wound healing efficacy of a novel CQDs@AgNPs@CS-based nanocomposites: A multifunctional approach for advanced wound care. *International Journal of Biological Macromolecules, 311*, Article 143621. https://doi.org/10.1016/j.ijbiomac.2025.143621

Emam, H. E. (2024). Carbon quantum dots derived from polysaccharides: Chemistry and potential applications. *Carbohydrate Polymers, 324*, Article 121503. https://doi.org/10.1016/j.carbpol.2023.121503

Fahimirad, S., Khaki, M., Ghaznavi-Rad, E., & Abtahi, H. (2024). Investigation of a novel bilayered PCL/PVA electrospun nanofiber incorporated chitosan-LL37 and chitosan-VEGF nanoparticles as an advanced antibacterial cell growth-promoting wound dressing. *International Journal of Pharmaceutics, 661*, Article 124341. https://doi.org/10.1016/j.ijpharm.2024.124341

Fu, Z., Zhang, L., Ren, M.-H., & BeMiller, J. N. (2019). Developments in Hydroxypropylation of starch: A review. *Starch - Stärke, 71*(1–2), Article 1800167. https://doi.org/10.1002/star.201800167

Han, W.-H., Wang, Q.-Y., Kang, Y.-Y., Shi, L.-R., Long, Y., Zhou, X., & Hao, C.-C. (2023). Cross-linking electrospinning. *Nanoscale, 15*(38), 15513–15551. https://doi.org/10.1039/D3NR03956K

Hong, F., Qiu, P., Wang, Y., Ren, P., Liu, J., Zhao, J., & Gou, D. (2024). Chitosan-based hydrogels: From preparation to applications, a review. *Food Chemistry: X, 21*, Article 101095. https://doi.org/10.1016/j.fochx.2023.101095

Hou, M., Xu, Q., Wang, L., Zhang, X., Zhang, L., Gao, H., & Liu, L. (2025). Nanocellulose/sodium alginate porous foams for enhanced wound healing and antibacterial properties. *International Journal of Biological Macromolecules, 320*, Article 146009. https://doi.org/10.1016/j.ijbiomac.2025.146009

Huang, D., Du, J., Luo, F., He, G., Zou, M., Wang, Y., … Weng, Z. (2024). Injectable hydrogels with integrated Ph probes and ultrasound-responsive microcapsules as smart wound dressings for visual monitoring and on-demand treatment of chronic wounds. *Advanced Healthcare Materials, 13*(9), Article 2303379. https://doi.org/10.1002/adhm.202303379

Ji, M., Li, J., Wang, Y., Li, F., Man, J., Li, J., Zhang, C., Peng, S., & Wang, S. (2022). Advances in chitosan-based wound dressings: Modifications, fabrications, applications and prospects. *Carbohydrate Polymers, 297*, Article 120058. https://doi.org/10.1016/j.carbpol.2022.120058

Ju, T., Li, J., Weston, A., Satta, G., Bolognini, S., Di Luca, M., … Williams, G. R. (2025). Anti-pseudomonas aeruginosa bacteriophage loaded electrospun fibers for antibacterial wound dressings. *Macromolecular Rapid Communications, 46*, 2400744. https://doi.org/10.1002/marc.202400744

Juncos Bombin, A. D., Dunne, N. J., & McCarthy, H. O. (2020). Electrospinning of natural polymers for the production of nanofibres for wound healing applications. *Materials Science & Engineering. C, Materials for Biological Applications, 114*, Article 110994. https://doi.org/10.1016/j.msec.2020.110994

Karthikeyan, L., & Wook Kang, H. (2025). Recent progress in multifunctional theranostic hydrogels: The cornerstone of next-generation wound care technologies. *Biomaterials Science, 13*(16), 4358–4389. https://doi.org/10.1039/D5BM00781J

Lee, D. U., Kim, S.-C., Choi, D. Y., Jung, W.-K., & Moon, M. J. (2023). Basic amino acid-mediated cationic amphiphilic surfaces for antimicrobial pH monitoring sensor with wound healing effects. *Biomaterials Research, 27*(1), Article 14. https://doi.org/10.1186/s40824-023-00355-0

Li, Y., Song, S., Song, J., Gong, R., & Abbas, G. (2025). Electrochemical pH sensor incorporated wearables for state-of-the-art wound care. *ACS Sensors*. https://doi.org/10.1021/acssensors.4c03408

Liu, F., Cao, Y., Ren, J., Xie, Y., Xiao, X., Zou, B., Zhang, X., & Chen, Y. (2025). Optimization of starch foam extrusion through PVA polymerization, moisture content control, and CMCS incorporation for enhanced antibacterial cushioning packaging. *Carbohydrate Polymers, 347*, Article 122763. https://doi.org/10.1016/j.carbpol.2024.122763

Liu, H., Yang, H., Zhu, K., Peng, F., Guo, L., & Qi, H. (2022). Facile fabrication of a polyvinyl alcohol-based hydrophobic fluorescent film via the Hantzsch reaction for broadband UV protection. *Materials Horizons, 9*(2), 815–824. https://doi.org/10.1039/D1MH01783G

Liu, L., Hu, G., Chen, L., & Hong, F. F. (2025). A microporous hemostatic and antibacterial multifunctional composite foam wound dressing derived from oxidized bacterial cellulose. *International Journal of Biological Macromolecules*. , Article 146928. https://doi.org/10.1016/j.ijbiomac.2025.146928

Liu, X., Rodeheaver, D. P., White, J. C., Wright, A. M., Walker, L. M., Zhang, F., & Shannon, S. (2018). A comparison of in vitro cytotoxicity assays in medical device regulatory studies. *Regulatory Toxicology and Pharmacology, 97*, 24–32. https://doi.org/10.1016/j.yrtph.2018.06.003

Liu, X., Yu, J., Tan, Y., Zhang, W., Zhu, L., Ye, S., & Feng, J. (2025). Engineering nitrogen-doped carbon quantum dots: Nitrogen content-controlled dual-phase emission behavior. *Journal of Colloid and Interface Science, 686*, 951–959. https://doi.org/10.1016/j.jcis.2025.02.024

Liu, Y., Li, T., Han, Y., Li, F., & Liu, Y. (2021). Recent development of electrospun wound dressing. *Current Opinion in Biomedical Engineering, 17*, Article 100247. https://doi.org/10.1016/j.cobme.2020.100247

Lohrasbi Nejad, S., & Shekarchizadeh, H. (2024). Visual tracking of real-time freshness of fish using an agar hydrogel colorimetric indicator containing CuNPs/NCQDs. *Carbohydrate Polymers, 343*, Article 122477. https://doi.org/10.1016/j.carbpol.2024.122477

Long, L., Liu, W., Hu, C., Yang, L., & Wang, Y. (2022). Construction of multifunctional wound dressings with their application in chronic wound treatment. *Biomaterials Science, 10*(15), 4058–4076. https://doi.org/10.1039/D2BM00620K

Madani, M., Cruz, C. D., Gounani, Z., Baniasadi, H., Tammela, P., Laaksonen, T., … Seppälä, J. (2025). Functionalized cellulose nanocrystals reinforced PLA-gelatin electrospun fibers for potential antibacterial wound dressing and coating applications. *International Journal of Biological Macromolecules, 287*, Article 138389. https://doi.org/10.1016/j.ijbiomac.2024.138389

Malavika, J. P., Shobana, C., Sundarraj, S., Ganeshbabu, M., Kumar, P., & Selvan, R. K. (2022). Green synthesis of multifunctional carbon quantum dots: An approach in cancer theranostics. *Biomaterials Advances, 136*, Article 212756. https://doi.org/10.1016/j.bioadv.2022.212756

Mariani, F., Serafini, M., Gualandi, I., Arcangeli, D., Decataldo, F., Possanzini, L., … Scavetta, E. (2021). Advanced wound dressing for real-time pH monitoring. *ACS Sensors, 6*(6), 2366–2377. https://doi.org/10.1021/acssensors.1c00552

Mary, S. K., Koshy, R. R., Arunima, R., Thomas, S., & Pothen, L. A. (2022). A review of recent advances in starch-based materials: Bionanocomposites, pH sensitive films, aerogels and carbon dots. *Carbohydrate Polymer Technologies and Applications, 3*, Article 100190. https://doi.org/10.1016/j.carpta.2022.100190

Minsart, M., Van Vlierberghe, S., Dubruel, P., & Mignon, A. (2022). Commercial wound dressings for the treatment of exuding wounds: An in-depth physico-chemical comparative study. *Burns & Trauma, 10*, Article tkac024. https://doi.org/10.1093/burnst/tkac024

Miyazaki, M., Van Hung, P., Maeda, T., & Morita, N. (2006). Recent advances in application of modified starches for breadmaking. *Trends in Food Science & Technology, 17*(11), 591–599. https://doi.org/10.1016/j.tifs.2006.05.002

Nauman, S., Lubineau, G., & Alharbi, H. F. (2021). Post processing strategies for the enhancement of mechanical properties of ENMs (electrospun Nanofibrous membranes): A review. *Membranes, 11*(1), 39. https://doi.org/10.3390/membranes11010039

Pallavolu, M. R., Prabhu, S., Nallapureddy, R. R., Kumar, A. S., Banerjee, A. N., & Joo, S. W. (2023). Bio-derived graphitic carbon quantum dot encapsulated S- and N-doped graphene sheets with unusual battery-type behavior for high-performance supercapacitor. *Carbon, 202*, 93–102. https://doi.org/10.1016/j.carbon.2022.10.077

Percival, S. L., McCarty, S., Hunt, J. A., & Woods, E. J. (2014). The effects of pH on wound healing, biofilms, and antimicrobial efficacy. *Wound Repair and Regeneration, 22*(2), 174–186. https://doi.org/10.1111/wrr.12125

Preethi, M., Murugan, R., Viswanathan, C., & Ponpandian, N. (2022). Potato starch derived N-doped carbon quantum dots as a fluorescent sensing tool for ascorbic acid. *Journal of Photochemistry and Photobiology A: Chemistry, 431*, Article 114009. https://doi.org/10.1016/j.jphotochem.2022.114009

Qi, S., Zhang, M., Guo, X., Yue, L., Wang, J., Shao, Z., & Xin, B. (2017). Controlled extracellular biosynthesis of ZnS quantum dots by sulphate reduction bacteria in the presence of hydroxypropyl starch as a mediator. *Journal of Nanoparticle Research, 19*(6), 212. https://doi.org/10.1007/s11051-017-3899-2

Rong, L., Liu, H., Wang, B., Mao, Z., Xu, H., Zhang, L., Zhong, Y., Feng, X., & Sui, X. (2019). Durable antibacterial and hydrophobic cotton fabrics utilizing enamine bonds. *Carbohydrate Polymers, 211*, 173–180. https://doi.org/10.1016/j.carbpol.2019.01.103

Sadeghi-Aghbash, M., Rahimnejad, M., Adeli, H., & Feizi, F. (2024). Catecholamines polymerization crosslinking for alginate-based burn wound dressings developed with ciprofloxacin and zinc oxide interactions. *International Journal of Biological Macromolecules, 260*, Article 129400. https://doi.org/10.1016/j.ijbiomac.2024.129400

Sharma, N., Das, G. S., & Yun, K. (2020). Green synthesis of multipurpose carbon quantum dots from red cabbage and estimation of their antioxidant potential and bio-labeling activity. *Applied Microbiology and Biotechnology, 104*(16), 7187–7200. https://doi.org/10.1007/s00253-020-10726-5

Shen, Z., Zhang, C., Wang, T., & Xu, J. (2023). Advances in functional hydrogel wound dressings: A review. *Polymers, 15*(9), Article 9. https://doi.org/10.3390/polym15092000

Shi, R., Zhu, Y., Chen, Y., Lin, Y., & Shi, S. (2024). Advances in DNA nanotechnology for chronic wound management: Innovative functional nucleic acid nanostructures for overcoming key challenges. *Journal of Controlled Release, 375*, 155–177. https://doi.org/10.1016/j.jconrel.2024.09.004

Sun, Q., Zhang, L., Huang, M., Ma, M., Zeng, J., & Le, T. (2024). Modification of starch-derived graphene quantum dots as multifunctional nanofillers to produce polymer starch/polyvinyl alcohol composite films for active packaging. *LWT, 198*, Article 115953. https://doi.org/10.1016/j.lwt.2024.115953

Sung, J. H., Hwang, M.-R., Kim, J. O., Lee, J. H., Kim, Y. I., Kim, J. H., … Choi, H.-G. (2010). Gel characterisation and *in vivo* evaluation of minocycline-loaded wound dressing with enhanced wound healing using polyvinyl alcohol and chitosan. *International Journal of Pharmaceutics, 392*(1), 232–240. https://doi.org/10.1016/j.ijpharm.2010.03.024

Tang, N., Zheng, Y., Jiang, X., Zhou, C., Jin, H., Jin, K., … Haick, H. (2021). Wearable sensors and systems for wound healing-related pH and temperature detection. *Micromachines, 12*(4), Article 4. https://doi.org/10.3390/mi12040430

Tauc, J., Grigorovici, R., & Vancu, A. (1966). Optical properties and electronic structure of amorphous germanium. *Physica Status Solidi B, 15*(2), 627–637. https://doi.org/10.1002/pssb.19660150224

Uberoi, A., McCready-Vangi, A., & Grice, E. A. (2024). The wound microbiota: Microbial mechanisms of impaired wound healing and infection. *Nature Reviews Microbiology, 22*(8), 507–521. https://doi.org/10.1038/s41579-024-01035-z

Versey, Z., da Cruz Nizer, W. S., Russell, E., Zigic, S., DeZeeuw, K. G., Marek, J. E., … Cassol, E. (2021). Biofilm-innate immune Interface: Contribution to chronic wound formation. *Frontiers in Immunology, 12*. https://doi.org/10.3389/fimmu.2021.648554

Wang, W., Wang, S., Xiang, C., Xue, D., Li, M., Liu, Q., Piao, L., & Wang, D. (2022). Nanofiber-based transparent film with controllable optical transparency adjustment function for versatile bionic applications. *Nano Research, 15*(1), 564–572. https://doi.org/10.1007/s12274-021-3521-x

Wang, Y., Yang, M., & Zhao, Z. (2023). Facile fabrication of self-healing, injectable and antimicrobial cationic guar gum hydrogel dressings driven by hydrogen bonds. *Carbohydrate Polymers, 310*, Article 120723. https://doi.org/10.1016/j.carbpol.2023.120723

Xiong, Y., Feng, Q., Lu, L., Qiu, X., Knoedler, S., Panayi, A. C., … Zhao, Y. (2024). Metal–organic frameworks and their composites for chronic wound healing: From bench to bedside. *Advanced Materials, 36*(2), Article 2302587. https://doi.org/10.1002/adma.202302587

Yang, Y., Zhang, C., Zhang, Z., Yu, F., Wang, Y., Ding, J., Zhao, Z., & Liu, Y. (2024). A pH responsive tannic acid/quaternized carboxymethyl chitosan/oxidized sodium alginate hydrogels for accelerated diabetic wound healing and real-time monitoring. *International Journal of Biological Macromolecules, 264*, Article 130741. https://doi.org/10.1016/j.ijbiomac.2024.130741

Yao, Y., Zhou, W., Cai, K., Wen, J., & Zhang, X. (2024). Advances in the study of the biological activity of polysaccharide-based carbon dots: A review. *International Journal of Biological Macromolecules, 281*, Article 135774. https://doi.org/10.1016/j.ijbiomac.2024.135774

Youssef, K., Ullah, A., Rezai, P., Hasan, A., & Amirfazli, A. (2023). Recent advances in biosensors for real time monitoring of pH, temperature, and oxygen in chronic wounds. *Materials Today Bio, 22*, Article 100764. https://doi.org/10.1016/j.mtbio.2023.100764

Zeng, Z., Zhu, M., Chen, L., Zhang, Y., Lu, T., Deng, Y., Ma, W., Xu, J., Huang, C., & Xiong, R. (2022). Design the molecule structures to achieve functional advantages of hydrogel wound dressings: Advances and strategies. *Composites Part B: Engineering, 247*, Article 110313. https://doi.org/10.1016/j.compositesb.2022.110313

Zhang, S., Gatsi, B., Yao, X., Jin, Y., & Amhal, H. (2025). Cellulose nanofiber-reinforced antimicrobial and antioxidant multifunctional hydrogel with self-healing, adhesion for enhanced wound healing. *Carbohydrate Polymers, 352*, Article 123189. https://doi.org/10.1016/j.carbpol.2024.123189

Zheng, K., Tong, Y., Zhang, S., He, R., Xiao, L., Iqbal, Z., … Li, Y. (2021). Flexible bicolorimetric polyacrylamide/chitosan hydrogels for smart real-time monitoring and promotion of wound healing. *Advanced Functional Materials, 31*(34), Article 2102599. https://doi.org/10.1002/adfm.202102599

Zhu, M., Zhang, S., Li, X., Xiao, C., & Wang, N. (2025). A crosslinked PVA/GO hydrogel for wound dressing with pH-controlled drug release capabilities. *Materials Today Communications, 43*, Article 111760. https://doi.org/10.1016/j.mtcomm.2025.111760

Zhu, Y., Zhang, J., Song, J., Yang, J., Du, Z., Zhao, W., … Zhang, L. (2020). A multifunctional pro-healing Zwitterionic hydrogel for simultaneous optical monitoring of pH and glucose in diabetic wound treatment. *Advanced Functional Materials, 30*(6), Article 1905493. https://doi.org/10.1002/adfm.201905493

Zong, Y., Zong, B., Zha, R., Zhang, Y., Li, X., Wang, Y., … Li, C. (2023). An antibacterial and anti-oxidative hydrogel dressing for promoting diabetic wound healing and real-time monitoring wound pH conditions with a NIR fluorescent imaging system. *Advanced Healthcare Materials, 12*(24), Article 2300431. https://doi.org/10.1002/adhm.202300431